ACS Catalysis

pubs.acs.org/acscatalysis

Research Article

Lavender-Like Ga-Doped Pt_3Co Nanowires for Highly Stable and Active Electrocatalysis

Menggang Li,[#] Zhonglong Zhao,[#] Zhonghong Xia, Yong Yang, Mingchuan Luo, Yarong Huang, Yingjun Sun, Yuguang Chao, Wenxiu Yang, Weiwei Yang, Yongsheng Yu,* Gang Lu,* and Shaojun Guo*

Cite This: *ACS Catal.* 2020, 10, 3018−3026

Read Online

ACCESS | Metrics & More | Article Recommendations | Supporting Information

ABSTRACT: One-dimensional (1D) PtM (M = Fe, Co, Ni) nanowires (NWs), which represent a thriving class of electrocatalysts for fuel cells, are experiencing a restriction in long-term durability because of the dissolving issue related to transition metals. Utilizing one-dimensional Pt_3Co NWs as the basic catalyst model, here we have successfully demonstrated significant improvements in electrocatalytic durability and activity derived from doping of Ga atoms. The optimized surface energy caused by the doping of Ga atoms drives the resulting catalysts to exhibit good durability for oxygen reduction reaction (ORR) electrocatalysis. However, although oxygen binding energy (E_O) would rather deviate from the optimal value because of excessive Ga on the surface, the formation of proper Ga−O bonding can also promote oxygen binding to approach an optimal value, which results in an enhanced ORR activity. It can be therefore concluded that doping of an appropriate amount of Ga atoms has a positive effect in improving the ORR performance of the catalyst, not only in terms of specific activity but also in durability. This interesting phenomenon was also further extended to improve the catalysis of methanol oxidation (MOR) and ethanol oxidation (EOR) reactions, thus reflecting multifunctionalities of lavender-like Ga-doped Pt_3Co NWs on fuel cell reactions. This study highlights the great potential of Ga-doped strategies for surface and near-surface regulation, which can effectively address the poor durability of 1D Pt-based NWs for energy catalytic technology.

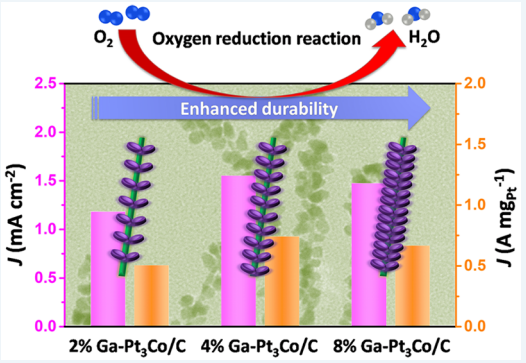

KEYWORDS: *one-dimensional nanostructures, Ga-doped, Pt_3Co, electrocatalysis, durability*

1. INTRODUCTION

Nowadays, with the rapid development of a sustainable economy and the massive consumption of fossil fuel resources, promising energy-conversion technologies have been stimulated and triggered. Polymer electrolyte membrane fuel cells (PEMFCs) can provide high energy density and conversion efficiency as well as wide operating temperatures, and thus, they are considered as a new class of promising energy conversion devices.[1−5] Pt, an ideal anode/cathode catalyst for PEMFCs, has actually hindered the implementation and commercialization of PEMFCs because of its high cost, intrinsically sluggish kinetics, and low durability of the cathode oxygen reduction reactions (ORR).[6−11] It is therefore particularly crucial to design low-cost, effective, and stable Pt-based alloy nanocatalysts for the cathode, which involves the regulation of microscopic morphology and dimensions, the rearrangement of Pt atoms on the surface, and favorable ligand and strain effects.[12−19] To bridge this gap, a wide variety of nanocrystals with well-defined dimensions, morphology, and compositional distributions have been synthesized, which can modulate the exposed facets and surface coordination environment.[16,20−30] Constructing one-dimensional (1D) Pt-based alloy nanomaterials, which have intrinsic anisotropic structure with high surface atoms utilization efficiency, is considered to be an effective approach to obtain high-performance cathode ORR electrocatalysts.[31−36] In spite of the considerable progress on enhancing the catalytic activities of Pt-based nanowires (NWs), a gap in durability for realizing the practical application still exists.[33,36−39] A critical issue is the instability of high surface energies for the exposed active facets including high-index facets (HIFs), especially during the long-term process, which thus necessitates further optimization of the surface and near-surface atomic structures to enhance the expected durability.[36,40−42] To address this severe challenge, heterogeneous atomic doping has been found to be an effective strategy, which can often provide advantages in stabilizing the initial morphology and the loss of transition metals.[43−46] Inspired by the aforementioned viewpoints, we are looking

Received: October 13, 2019
Revised: January 11, 2020
Published: January 16, 2020

https://dx.doi.org/10.1021/acscatal.9b04419
ACS Catal. 2020, 10, 3018−3026

forward to achieving superior active and stable electrocatalysts by integrating the features of Ga atoms' doping and unique anisotropic 1D nanostructures.

Herein, we utilized the surface Ga atoms-doped strategy and corresponding surface engineering of 1D Pt_3Co NWs to address this durability difficulty. We can obtain the highest specific activity and mass activity, which are 7.8 times and 6.3 times higher than those of the commercial Pt/C, respectively, for the optimized 4% Ga−Pt_3Co/C. In addition, more Ga content (8% Ga−Pt_3Co/C) can make it significantly stable toward ORR with almost no activity decrease after a 20 000-cycles durability test. We can attribute this contribution to the decrease of surface energy and the formation of Ga−O bindings caused by the surface doping of Ga atoms. Furthermore, similar results are also observed in both methanol oxidation (MOR) and ethanol oxidation (EOR) reactions, which further extend the multifunctional catalytic properties of lavender-like Ga-doped Pt_3Co NWs.

2. EXPERIMENTAL SECTION

2.1. Synthesis of Lavender-Like Ga-Doped Pt_3Co NWs. Before synthesis, $Ga(acac)_3$ was dissolved into OAm to obtain a clear solution (0.4 mg mL^{-1}). In a typical synthesis of 4% Ga−Pt_3Co NWs, $Pt(acac)_2$ (10 mg), $Co(acac)_3$ (8.9 mg), Glu (60 mg), CTAC (32 mg), and the above-mentioned solution (1 mL) were added into a glass vessel (20 mL). Then the solvent was added to 5 mL, followed by ultrasonicating for around 1 h. The resulting homogeneous mixed solution was soaked in an oil bath of 180 °C for 12 h and allowed naturally cool. The obtained black products were centrifuged with ethanol and washed for several times with the mixture of cyclohexane and ethanol. The final products were dispersed in cyclohexane (10 mL) for further experimentation. The synthesis of 2% Ga−Pt_3Co NWs and 8% Ga−Pt_3Co NWs was achieved by changing the amounts of $Ga(acac)_3$/OAm solution to 0.5 and 2 mL, respectively, while keeping the other parameters constant.

2.2. Synthesis of 4% Ga-Doped Pt_3Co Nanoparticles (NPs) and Pt_3Co NWs. The 4% Ga−Pt_3Co NPs were synthesized via the similar method to 4% Ga−Pt_3Co NWs, except for the absence of Glu and CTAC. For the synthesis of zigzag-like Pt_3Co NWs, the reactants do not contain the Ga precursors, while the other reaction conditions are unchanged.

2.3. Characterization. Transmission electron microscopy (TEM) and high-resolution TEM (HRTEM) images were obtained on a HITACHI H-7700 operating at 100 kV and FEI Tecnai G2 operating at 200 kV, respectively. Power X-ray diffraction (PXRD) patterns were recorded on a PANalytical-XRD instrument using Cu Kα radiation (λ = 0.15406 nm) at 40 kV. Scanning electron microscopy-energy dispersive X-ray spectroscopy (SEM-EDS) spectra were probed with an EDS detector system attached to JEOL JSM-6360. High-resolution X-ray photoelectron spectroscopy (XPS) spectra were collected on a XPS instrument from Thermo Scientific (ESCALAB 250 XI). The quantitatively elemental analysis of catalysts was determined by inductively coupled plasma atomic emission spectroscopy (ICP-AES) on an Agilent 8800 instrument.

2.4. Electrochemical Measurements. All the electrochemical measurements were tested on a CHI 760E (Chenhua, Shanghai) electrochemical workstation, and all recorded relevant potentials were converted to a reversible hydrogen electrode (RHE). Before the electrochemical tests, the as-synthesized Ga-doped Pt_3Co NWs were deposited on Ketjen Black-300J (carbon supports). Specifically, the obtained samples dispersed in cyclohexane (10 mL) and carbon supports dispersed in ethanol (50 mL) were first mixed and then sonicated for 3 h. Subsequently, the black products were centrifuged for collection. Then, the products were redispersed in acetic acid (36%) and heated at 60 °C for 2 h under N_2 flowing for the purpose of removing the residual organic impurities. Finally, the products were washed with ethanol for three times. The final catalysts were obtained by drying the products. Afterward, the catalysts were dispersed in the solution containing isopropyl alcohol, ultrapure water, and a Nafion solution (volume ratio is 1:1:0.008) to obtain the catalysts ink (1 mg mL^{-1}). The dispersion (10 μL) was dropped onto the rotating disk glassy carbon electrode (RDE, 5 mm) to obtain the working electrode. The Pt mass of each electrode was quantified by ICP-AES measurement.

All the electrochemical experiments were conducted with a conventional three-electrode configuration at room temperature, where a catalyst modified RDE, Pt foil (1.5 cm × 1 cm), and saturated calomel electrode (SCE) were used as the working, counter, and reference electrodes, respectively. Cyclic voltammograms (CVs) were performed in N_2-saturated 0.1 M $HClO_4$ at a sweep rate of 50 mV s^{-1}, and electrochemically active surface areas (ECSAs) were derived on the basis of the desorption charge of underpotentially deposited hydrogen (H_{upd}), which assume that the charge density of a monolayer of adsorbed hydrogen is 210 C cm^{-2}. The ORR polarization curves were tested in O_2-saturated 0.1 M $HClO_4$ at a sweep rate of 20 mV s^{-1} and a rotation rate of 1600 rpm without *iR*-correction. The accelerated durability tests (ADTs) were carried out by conducting the CVs between 0.6 and 1.1 V versus RHE for 20 k cycles with a scan rate of 100 mV s^{-1}.

The MOR measurements were tested in N_2-saturated 0.1 M $HClO_4$ solution containing 0.5 M methanol at a sweep rate of 50 mV s^{-1}. For MOR stability testing, the chronoamperometric curves were conducted at 0.65 V versus RHE for a period of 5000 s. In addition, the EOR measurements were performed the same as those of the MOR, except that the alcohol molecule was changed from methanol to ethanol. All the specific activities and mass activities were determined by normalizing the kinetic current densities to ECSAs and real amount of Pt loading.

2.5. Density Functional Theory (DFT) Calculations. Typically, the surface energy of Pt (111), Pt_3Co, and Ga−Pt_3Co was calculated as $E_{surf}(Pt) = (E_{slab} - N_{Pt}E_{Pt})/2A$, $E_{surf}(Pt_3Co) = (E_{slab} - N_{Pt}E_{Pt} - N_{Co}E_{Co})/2A$ and $E_{surf}(Ga-Pt_3Co) = (E_{slab} - N_{Pt}E_{Pt} - N_{Co}E_{Co} - N_{Ga}E_{Ga})/2A$,[47] respectively, where E_{slab} represents the total energy of the slab; E_{Pt}, E_{Co}, and E_{Ga} represent the atomic energy of Pt, Co, and Ga in their bulk phases, respectively. N_{Pt}, N_{Co}, and N_{Ga} represent the number of Pt, Co, and Ga atoms in the slab, respectively. A represents the surface area of the slab. The oxygen binding energy E_O was calculated as $E_O = E_{surf+O} - E_{surf} - 1/2E_{O_2}$, where E_{surf+O} and E_{surf} represent the total energies of the surface with and without the oxygen adsorbate, respectively. E_{O_2} represents the total energy of an oxygen molecule. A four-layer slab model was used to simulate the Pt (111), Pt_3Co, and Ga−Pt_3Co surfaces. A vacuum layer of 15 Å is added to the adjacent slabs. DFT calculations were conducted using the Vienna ab initio simulation package (VASP).[48] The Perdew−Burke−Ernzerhof (PBE) functional

https://dx.doi.org/10.1021/acscatal.9b04419
ACS Catal. 2020, 10, 3018−3026

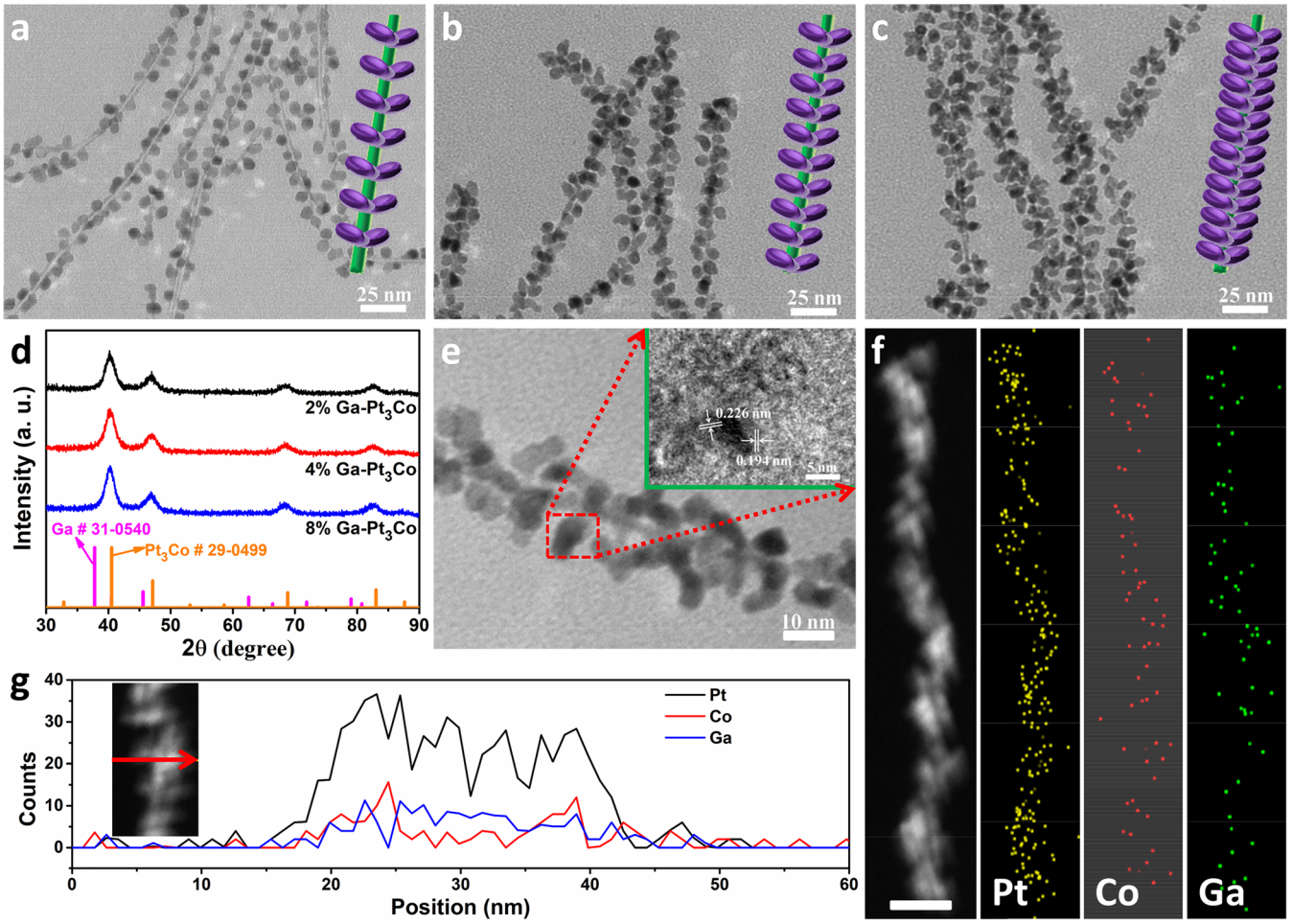

Figure 1. Structure and compositional characterization of lavender-like Ga-doped Pt_3Co NWs. Representative TEM images of (a) 2% Ga−Pt_3Co, (b) 4% Ga−Pt_3Co, and (c) 8% Ga−Pt_3Co NWs (the insets are the corresponding schematic illustration). (d) PXRD patterns of different Ga-doped Pt_3Co NWs. (e) HRTEM image, (f) STEM-EDS elemental mapping images (the scale bar is 25 nm), and (g) elemental line-scan across the red arrow in the inset of the single 4% Ga−Pt_3Co NW.

within the generalized gradient approximation was used to describe the exchange-correlation functional.[49,50] The energy cutofff of the plane-wave basis set was taken as 400 eV, and the Brillouin zone was sampled with a 3 × 3 × 1 k-point mesh on the basis of the Monkhorst−Pack scheme.[51] The force convergence criterion for atomic relaxation was 0.02 eV $Å^{-1}$.

3. RESULTS AND DISCUSSION

By tuning the precursor amount of $Ga(acac)_3$ in the reactants, the Ga-doped Pt_3Co NWs with different Ga composition can be obtained. The NPs covered on the surface of NWs become denser with the increase of Ga content, thereby forming a dense lavender-like structure with leaves of ∼10 nm and stems of ∼1 nm in diameter (Figure 1a−c and Figure S1, Supporting Information). The successful reduction of Pt, Co, and Ga can be confirmed by SEM-EDS spectra and ICP-AES, and the molar ratios of Pt/Co/Ga among the three different structure of the samples are 73/25/2, 72/24/4, and 69/23/8, respectively (Figure S2), thus termed as 2% Ga−Pt_3Co, 4% Ga−Pt_3Co, and 8% Ga−Pt_3Co, respectively. The PXRD patterns (Figure 1d) of the NWs show several diffraction peaks, which can be assigned to face-centered cubic (fcc) phases. The positions of all characteristic diffraction peaks are shifted to lower angles relative to the corresponding diffraction peaks of Pt_3Co (Pt_3Co, JCPDS No. 29-0499) with the unit cell size of 0.3854 × 0.3854 × 0.3854 nm (Figure S3), which is consistent with the increased lattice spacing resulting from the surface-doping of Ga atoms into NWs. The HRTEM image of PtCoGa nanoparticles on the surface of NWs is displayed in Figure 1e and the inset, where the spacings of the lattice measured to be 0.226 and 0.194 nm correspond to the (111) and (200) crystal facets of 4% Ga−Pt_3Co, respectively, slightly larger than those of Pt_3Co (0.222 and 0.192 nm). Moreover, the scanning TEM energy-dispersive X-ray spectroscopy (STEM-EDX) elemental mapping (Figure 1f) of a single 4% Ga−Pt_3Co NW further confirms the existence of Pt, Co, and Ga throughout the whole NW. The detailed distribution of elements was further characterized by line-scan analysis, as shown in Figure 1g. It is apparent that Pt is mainly distributed across the whole portion of the lavender-like Ga-doped Pt_3Co NWs, while Co is distributed in the outside of NWs, which means that the stem of lavender-like Ga-doped Pt_3Co NWs is composed of PtGa and the surface leaves are composed of PtCoGa. The high-resolution XPS spectra further confirm the presence of Pt, Co, and Ga elements in the lavender-like Ga-doped Pt_3Co NWs, where Pt exists mainly in metallic state, while Co and Ga are in the oxidized state (Figure S4). Note that the Ga is in a Ga^{3+} state (Ga_2O_3), which can be demonstrated by both Ga 2p and Ga 3d peaks. The surface Ga

https://dx.doi.org/10.1021/acscatal.9b04419
ACS Catal. 2020, 10, 3018−3026

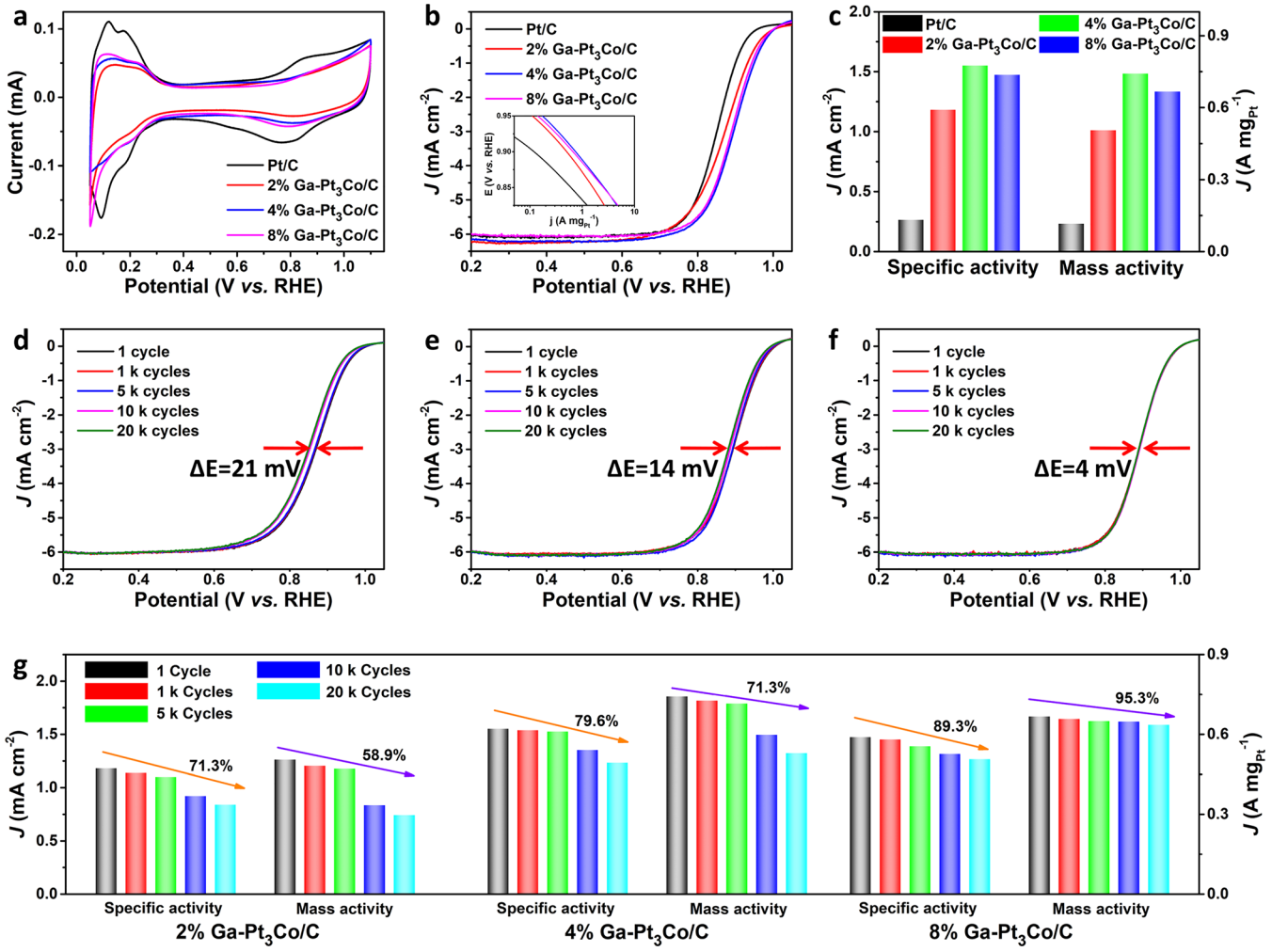

Figure 2. ORR performance of different Ga-doped Pt_3Co NWs and commercial Pt/C catalysts in 0.1 M $HClO_4$. (a) The CVs, (b) ORR polarization curves (inset is the Tafel plots of mass activities), (c) ORR specific activities and mass activities at 0.9 V versus RHE. ORR polarization curves of (d) 2% Ga−Pt_3Co/C, (e) 4% Ga−Pt_3Co/C, and (f) 8% Ga−Pt_3Co/C and (g) the ORR specific activities and mass activities at 0.9 V versus RHE before and after different potential cycles.

atoms content is measured to be 4%, which is close to the ICP-AES results, indicating the Ga atoms are mainly distributing on the surface of NWs. The models in the insets of Figure 1a−c vividly represent the changes in the PtGa/PtCoGa core/shell structure of lavender-like Ga-doped Pt_3Co NWs.

The structures of lavender-like Ga-doped Pt_3Co NWs can be controlled by adjusting the initial formation of seed crystals and subsequent kinetic growth, which can be achieved by varying the amount of CTAC (as structure-directing agent and surfactant) and Glu (as reductant) (Figures S5 and S6). The products tend to form 1D structure due to the presence of CTAC, and Glu can always control the growth rate of the nanocrystals. A low concentration of Glu can make the NPs on the surface of NWs sparse, similar to the structure of 2% Ga−Pt_3Co NWs, implying the amount of $Ga(acac)_3$ also can regulate the growth rate of NWs. Similarly, by increasing the amount of Glu or $Ga(acac)_3$, the structure of NWs would be destroyed because of the rapid growth of the crystal nucleus (Figure S7). In addition, a suitable feed ratio of Pt/Co precursors also plays an essential role in controlling the morphology of the final products (Figures S8 and S9). More notably, the NPs on the surface will be loose by reducing the content of Co atoms, further implying that the shells were made of PtCoGa (Figure S9a,b).

In this wet-chemical synthesis system, the growth mechanism of lavender-like Ga-doped Pt_3Co NWs can be attributed to three stages, which involves the initial formation of ultrathin Pt-rich NWs, the further attachment of NPs caused by slow reduction of metallic atoms, and the final process of growing up (Figure S10). In order to further elucidate this formation process, the intermediates collected at different reaction stages were further analyzed, and the evolution process was visualized via TEM images (Figure S11) and SEM-EDS spectra (Figure S12). Specifically, ultrathin Ga-doped Pt NWs are preferentially formed, indicating a faster reduction of Pt ions and preferential adsorption of Ga atoms, which is due to the higher standard reduction potential of Pt^{2+}/Pt (+1.19 V) and subsequent autocatalytic surface reduction mechanism.[52] At the next stage, rather, the Co species are reduced together with Pt and Ga into NPs and deposited on the Ga-doped Pt NWs surface, which indicates that the shell of NWs may be made of Pt, Co, and Ga. These results are in line with the conclusion of the line-scan profile (Figure 1g). Finally, the NPs gradually form densely into lavender-like NWs.

https://dx.doi.org/10.1021/acscatal.9b04419
ACS Catal. 2020, 10, 3018−3026

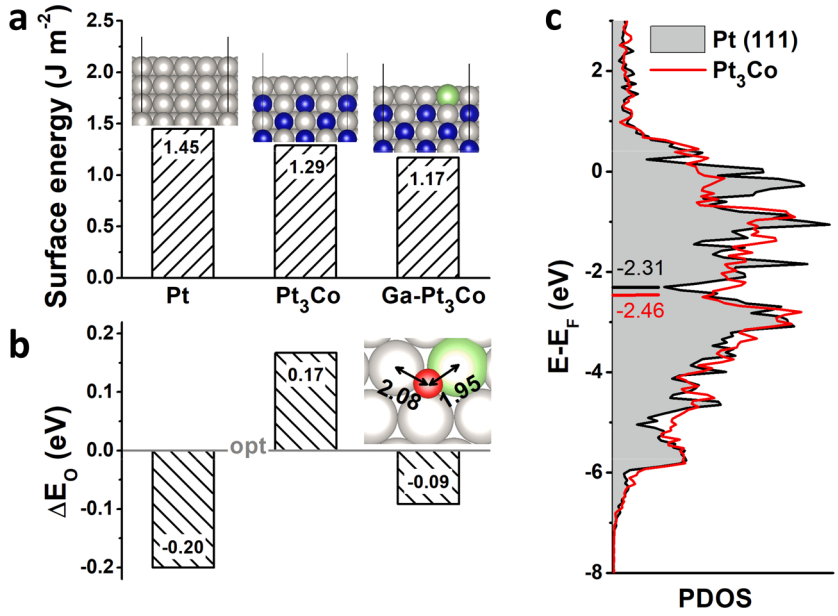

Figure 3. DFT calculations. (a) Surface energy and (b) ΔE_O of the pure Pt, Pt_3Co, and Ga-doped Pt_3Co (111) surfaces. The optimal E_O is set to 0. The computational models are shown in insets: gray, blue, green, and red spheres represent Pt, Co, Ga, and O atoms, respectively. (c) The partial density of states (PDOS) for the 3d band of the Pt atoms in the pure Pt and Pt_3Co surfaces, respectively. The horizontal lines indicate the calculated d-band centers.

The as-prepared NWs were used as electrocatalysts toward the ORR, MOR, and EOR. To carry out the electrochemical measurements, the NWs were loaded on the Ketjen Black-300J through sonicating. All the NWs can be homogeneously loaded on the carbon support with no structural changes (Figure S13, denoted as 2% Ga−Pt_3Co/C, 4% Ga−Pt_3Co/C, and 8% Ga−Pt_3Co/C, respectively). The CV curves of different Ga-doped Pt_3Co NWs and commercial Pt/C catalysts were conducted in N_2-saturated 0.1 M $HClO_4$ electrolyte at room temperature (Figure 2a). The ECSAs of 2% Ga−Pt_3Co/C, 4% Ga−Pt_3Co/C, 8% Ga−Pt_3Co/C, and Pt/C are derived to 45.9, 47.9, 54.3, and 59.2 $m^2\ g^{-1}$, respectively. Figure 2b shows the forward-scanned ORR polarization curves of different Ga-doped Pt_3Co NWs and commercial Pt/C catalysts in O_2-saturated 0.1 M $HClO_4$ electrolyte, and the rotation rate was set to 1600 rpm. Compared with the polarization curve of commercial Pt/C, all Ga-doped Pt_3Co/C catalysts show a severe positive shift, in which 4% Ga−Pt_3Co/C exhibits the highest half-wave potential ($E_{1/2}$) of 0.894 V, higher than 2% Ga−Pt_3Co/C (0.870 V) and 8% Ga−Pt_3Co/C (0.890 V), and even 43 mV higher than that of Pt/C. The intrinsic ORR activities were further quantitatively compared according to the Tafel plots. The 4% Ga−Pt_3Co/C delivers the highest mass activity at 0.9 V versus RHE (the inset in Figure 2b). Specifically, 4% Ga−Pt_3Co/C can deliver the ORR specific and mass activities of 1.56 mA cm^{-2} and 0.75 A mg_{Pt}^{-1}, 5.8 times and 6.3 times higher than those of Pt/C, respectively (Figure 2c). Both 2% Ga−Pt_3Co/C and 8% Ga−Pt_3Co/C, however, exhibit lower ORR activities (1.18 mA cm^{-2}, 0.51 A mg_{Pt}^{-1} and 1.48 mA cm^{-2}, 0.67 A mg_{Pt}^{-1}, respectively), suggesting that excessive incorporation of Ga atoms would inhibit the activity of the NWs catalysts. To highlight the advantages of such particular 1D nanostructures, we also synthesized the 4% Ga-doped Pt_3Co NPs, which possess the same irregular particle shape as the leaves of lavender-like Ga-doped Pt_3Co NWs (Figure S14). The Ga-doped Pt_3Co NPs catalysts only exhibit the specific activity of 0.67 mA cm^{-2} and mass activity of 0.32 A mg_{Pt}^{-1} at 0.9 V versus RHE, considerably lower than those of NWs (Figure S15). In addition, Pt_3Co NWs were further synthesized and supported on the carbon supports to compare the ORR performance, which also emphasizes the essential role of Ga atoms in this enhanced catalytic system (Figure S16). The specific details are summarized in the Table S1.

The ORR durability of electrocatalysts was examined with ADTs by 20 k potential cycles in O_2-saturated 0.1 M $HClO_4$. After ADTs, the $E_{1/2}$ of 2% Ga−Pt_3Co/C and 4% Ga−Pt_3Co/C shift negatively by 21 and 14 mV, while 8% Ga−Pt_3Co/C undergoes a negative shift of $E_{1/2}$ by only 4 mV (Figure 2d−f). CVs of the three catalysts before and after different cycles were tested to assess the loss of ECSAs after the ADTs (Figure S17). Notably, 8% Ga−Pt_3Co/C retains the highest proportion (92.7%) of the initial ECSA value, followed by 4% Ga−Pt_3Co/C (86.4%) and 2% Ga−Pt_3Co/C (76.9%). The enhanced durability of electrocatalysts was also manifested by comparing the specific and mass activities at 0.9 V versus RHE before and after ADTs (Figure 2g). The 8% Ga−Pt_3Co/C retains 89.3% of its initial specific activity after ADTs, whereas 4% Ga−Pt_3Co/C (79.6%) and 2% Ga−Pt_3Co/C C (71.3%) show inferior durability. In addition, 8% Ga−Pt_3Co/C also exhibits remarkable retained mass activity (95.3%) than 4% Ga−Pt_3Co/C (71.3%) and 2% Ga−Pt_3Co/C (58.9%). Furthermore, the well-maintained NWs structure and a negligible decrease of Co content can be obviously observed after 20 k cycles for 4% Ga−Pt_3Co/C (Figure S18). Furthermore, the Ga-doped Pt_3Co NPs and Pt_3Co NWs show instability compared with these lavender-like Ga-doped Pt_3Co NWs catalysts (Figure S19). All these results collectively point to the conclusion that Ga atoms have a positive impact on improving the ORR performance of the NWs catalysts, not only the specific activities, especially in terms of stability.

DFT calculations were further carried out to provide views into the origin of the enhanced ORR durability and activity of the Ga-doped Pt_3Co NWs. More specifically, the surface energy of the Ga-doped Pt_3Co (111) surface was calculated

https://dx.doi.org/10.1021/acscatal.9b04419
ACS Catal. 2020, 10, 3018−3026

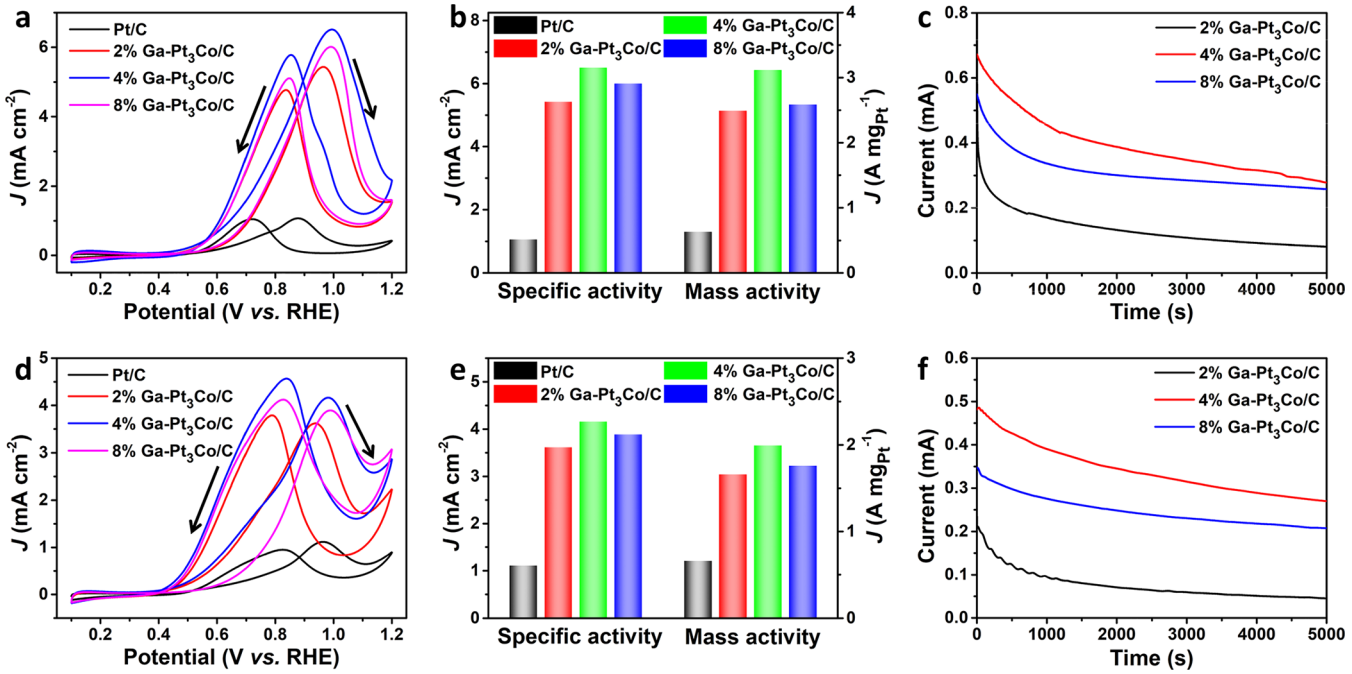

Figure 4. MOR and EOR performances of different Ga-doped Pt_3Co NWs and commercial Pt/C catalysts in 0.1 M $HClO_4$ containing 0.5 M CH_3OH or 0.5 M CH_3CH_2OH. (a) ECSA-normalized CVs, (b) specific activities and mass activities, and (c) $i-t$ curves for MOR. (d) ECSA-normalized CVs, (e) specific activities and mass activities, and (f) $i-t$ curves for EOR.

and further compared to the pure Pt and Pt_3Co (111) surfaces (Figure 3a). Surface energy represents an approximate measure of surface energetic stability, and the lower the surface energy, the more stable the surface. Four-atomic-layer slab models (with 64 atoms) were constructed for the DFT calculations. On the Pt_3Co surface, the top layer is of single Pt, while the remaining layers are composed of Pt_3Co alloy with 25% of Co, consistent with the experiment. To model the Ga-doped Pt_3Co surface, one of the surface Pt atoms in the slab model was replaced by a Ga atom, resulting in an approximate atomic composition of Ga at ~2%, also consistent with the experimental data. The surface energy of the Pt_3Co surface can be calculated to be 1.29 J m^{-2}, 11% lower than that of the pure Pt surface (1.45 J m^{-2}), suggesting that the former is energetically more stable than the latter. Interestingly, doping of Ga into the Pt_3Co surface further lowers its surface energy to 1.17 J m^{-2}, rendering the Ga-doped Pt_3Co surface even more stable. Therefore, the surface energy data could explain the experimental observations on the stability of the catalysts. Our conclusion of reduced surface energy in Ga-doped Pt_3Co NWs is consistent with a recent finding that strong Pt d and Ga p orbital hybridizations in PtGa alloy NWs could give rise to exceptional long-term durability of the PtGa NWs.[52]

In order to probe the ORR activity, we focused on oxygen binding energy (E_O) on the surface of catalysts. E_O can be used as an alternative for ORR activity on transition metal catalysts, and there is an optimal E_O value at which the ORR activity can reach the maximum.[53] We have calculated E_O on the (111) surfaces of pure Pt, Pt_3Co, and Ga-doped Pt_3Co NWs, respectively, based on the same slab models. For convenience, in Figure 3b, we use ΔE_O to show the difference of a given E_O value relative to the best reference. Since the Pt (111) surface binds 0.2 eV too strongly with oxygen,[54] its value of ΔE_O = −0.2 eV (ΔE_O = 0 corresponds to the optimal oxygen binding energy). By alloying with Co, the overbinding of oxygen on Pt is relieved thanks to charge transfer from Co to Pt (~0.61 electron per Co atom), which lowers the d-band center by 0.15 eV, (Figure 3c). As a result, E_O of the Pt_3Co surface shifts closer to the optimal value, implying an enhanced ORR activity than the pure Pt. However, ΔE_O now turns positive (ΔE_O = 0.17 eV), indicating that on the Pt_3Co surface, oxygen binding becomes too weak. Interestingly, doping of Ga onto the Pt_3Co surface can significantly increase the oxygen binding owing to the formation of strong Ga−O bonding, which can be confirmed by the XPS spectra of both Ga 2p and 3d (Figure S4c, d). Noticeably, the Ga−O bond length is calculated as 1.95 Å, shorter than the Pt−O bond length (2.08 Å), and ΔE_O of the Ga-doped Pt_3Co surface is found as −0.09 eV, much closer to the optimal value. Hence, the Ga-doped Pt_3Co surface should indeed have much higher ORR activities as observed in the experiments. We note that because of the strong binding of oxygen to the Ga atoms on the surface, excessive Ga content on the surface can eventually drive E_O away from the optimal value, thus decreasing the ORR activity. However, the surface stability should remain high due to Ga-reduced surface energies, consistent with the experimental results.

To explore the generality of Ga−Pt_3Co/C as highly efficient catalyst for fuel cells, the alcohol oxidation performances were further investigated. MOR activities were evaluated by conducting CVs at a scan rate of 50 mV s^{-1} in 0.1 M $HClO_4$ containing 0.5 M CH_3OH from 0.1 to 1.2 V versus RHE. The anodic currents for MOR of three Ga−Pt_3Co/C electrocatalysts are found to be much higher than that of Pt/C, and again, 4% Ga−Pt_3Co/C is appreciably active relative to 2% Ga−Pt_3Co/C and 8% Ga−Pt_3Co/C in terms of MOR catalytic performance (Figure 4a and Figure S20a). More impressively, the 4% Ga−Pt_3Co/C achieves 6.1 times higher in specific activity and 4.9 times higher in mass activity than Pt/C, respectively (Figure 4b and Table S2). The MOR stabilities of

https://dx.doi.org/10.1021/acscatal.9b04419
ACS Catal. 2020, 10, 3018−3026

catalysts were further recorded by $i-t$ curves (Figure 4c). Obviously, the anode current of 4% Ga−Pt_3Co/C is always higher than the other catalysts during the recording of 5000 s, indicating it has the most outstanding MOR performance. On the contrary, the 8% Ga−Pt_3Co/C can retain 46.9% of the initial current for MOR, superior to 2% Ga−Pt_3Co/C and 4% Ga−Pt_3Co/C, indicating the best durability of 8% Ga−Pt_3Co/C.

The catalytic activities for EOR were also assessed in 0.1 M $HClO_4$ containing 0.5 M CH_3CH_2OH (Figure 4d and Figure S20b). The 4% Ga−Pt_3Co/C also delivers the highest electrocatalytic activity, with a specific activity of 4.2 mA cm^{-2} and a mass activity of 2.0 A mg^{-1}, respectively (Figure 4e and Table S3). Furthermore, the 8% Ga−Pt_3Co/C displays a retention of 59.8% of the initial current for EOR, which is noticeably better than 2% Ga−Pt_3Co/C (20.6%) and 4% Ga−Pt_3Co/C (54.1%) (Figure 4f).

4. CONCLUSIONS

In summary, a surface Ga-doped strategy was presented to enhance the durability and activity for ORR of Pt_3Co NWs. As-prepared Ga-doped Pt_3Co NWs show a lavender-like core−shell structure, containing a stem composed of PtGa and surface leaves composed of PtCoGa. The optimized 4% Ga−Pt_3Co/C exhibits the highest activity (specific activity and mass activity are 1.56 mA cm^{-2} and 0.75 A mg_{Pt}^{-1} at 0.9 V versus RHE, respectively). On the other hand, the 8% Ga−Pt_3Co/C induces more outstanding durability (the half-wave potential only undergoes a negative shift of 4 mV after 20 k cycles). DFT calculations results indicate that the surface Ga-doping protocol tends to reduce the surface energy of Pt_3Co nanowires, which can drastically enhance the durability during the long-term cycles, and suitable Ga doping contents can generate Ga−O bondings to improve activity. We also demonstrated the favorable multifunctional catalytic properties of lavender-like Ga-doped Pt_3Co NWs for MOR and EOR. This study proposes a typical doping strategy for obtaining high-performance of promising one-dimensional Pt-based NWs via rational surface engineering, with particular emphasis on the essential role of Ga in achieving superior durability.

■ ASSOCIATED CONTENT

Supporting Information

The Supporting Information is available free of charge at https://pubs.acs.org/doi/10.1021/acscatal.9b04419.

Additional experimental section, images, and data of Figures S1−S19 and Tables S1−S3 as described in the text (PDF)

■ AUTHOR INFORMATION

Corresponding Authors

Yongsheng Yu − *MIIT Key Laboratory of Critical Materials Technology for New Energy Conversion and Storage, School of Chemistry and Chemical Engineering, Harbin Institute of Technology, Harbin, Heilongjiang 150001, China;* orcid.org/0000-0002-3907-693X; Email: ysyu@hit.edu.cn

Gang Lu − *Department of Physics and Astronomy, California State University Northridge, Northridge, California 91330, United States*; Email: ganglu@csun.edu

Shaojun Guo − *Department of Materials Science & Engineering, College of Engineering and BIC-ESAT, College of Engineering, Peking University, Beijing 100871, China;* orcid.org/0000-0003-4427-6837; Email: guosj@pku.edu.cn

Authors

Menggang Li − *Department of Materials Science & Engineering, College of Engineering, Peking University, Beijing 100871, China; MIIT Key Laboratory of Critical Materials Technology for New Energy Conversion and Storage, School of Chemistry and Chemical Engineering, Harbin Institute of Technology, Harbin, Heilongjiang 150001, China*

Zhonglong Zhao − *School of Physical Science and Technology, Inner Mongolia University, Hohhot 010021, China;* orcid.org/0000-0002-2245-9045

Zhonghong Xia − *Department of Materials Science & Engineering, College of Engineering, Peking University, Beijing 100871, China*

Yong Yang − *Department of Materials Science & Engineering, College of Engineering, Peking University, Beijing 100871, China*

Mingchuan Luo − *Department of Materials Science & Engineering, College of Engineering, Peking University, Beijing 100871, China*

Yarong Huang − *MIIT Key Laboratory of Critical Materials Technology for New Energy Conversion and Storage, School of Chemistry and Chemical Engineering, Harbin Institute of Technology, Harbin, Heilongjiang 150001, China*

Yingjun Sun − *Department of Materials Science & Engineering, College of Engineering, Peking University, Beijing 100871, China*

Yuguang Chao − *Department of Materials Science & Engineering, College of Engineering, Peking University, Beijing 100871, China*

Wenxiu Yang − *Department of Materials Science & Engineering, College of Engineering, Peking University, Beijing 100871, China*

Weiwei Yang − *MIIT Key Laboratory of Critical Materials Technology for New Energy Conversion and Storage, School of Chemistry and Chemical Engineering, Harbin Institute of Technology, Harbin, Heilongjiang 150001, China*

Complete contact information is available at: https://pubs.acs.org/10.1021/acscatal.9b04419

Author Contributions

#(M.L., Z.Z.) These authors contributed equally to this work.

Notes

The authors declare no competing financial interest.

■ ACKNOWLEDGMENTS

This study was financially supported by the Tencent Foundation through the XPLORER PRIZE, National Key R&D Program of China (No. 2016YFB0100201), the Beijing Natural Science Foundation (JQ18005), National Natural Science Foundation of China (Nos. 51671003 and 21802003), the China Postdoctoral Science Foundation (Nos. 2018M631239 and 2019TQ0001) and BIC-ESAT funding. The work at California State University Northridge was supported by the National Science Foundation PREM program (DMR-1828019).

■ REFERENCES

(1) Debe, M. K. Electrocatalyst Approaches and Challenges for Automotive Fuel Cells. *Nature* **2012**, *486*, 43−51.

(2) Wang, Y. J.; Zhao, N.; Fang, B.; Li, H.; Bi, X. T.; Wang, H. Carbon-Supported Pt-Based Alloy Electrocatalysts for the Oxygen Reduction Reaction in Polymer Electrolyte Membrane Fuel Cells: Particle Size, Shape, and Composition Manipulation and Their Impact to Activity. *Chem. Rev.* **2015**, *115*, 3433−3467.
(3) Wang, W.; Lei, B.; Guo, S. Engineering Multimetallic Nanocrystals for Highly Efficient Oxygen Reduction Catalysts. *Adv. Energy Mater.* **2016**, *6*, 1600236.
(4) Lin, R.; Cai, X.; Zeng, H.; Yu, Z. Stability of High-Performance Pt-Based Catalysts for Oxygen Reduction Reactions. *Adv. Mater.* **2018**, *30*, 1705332.
(5) Liang, J.; Ma, F.; Hwang, S.; Wang, X.; Sokolowski, J.; Li, Q.; Wu, G.; Su, D. Atomic Arrangement Engineering of Metallic Nanocrystals for Energy-Conversion Electrocatalysis. *Joule* **2019**, *3*, 956−991.
(6) Gasteiger, H. A.; Markovic, N. M. Just a Dream—or Future Reality? *Science* **2009**, *324*, 48−49.
(7) Mistry, H.; Varela, A. S.; Kühl, S.; Strasser, P.; Cuenya, B. R. Nanostructured Electrocatalysts with Tunable Activity and Selectivity. *Nat. Rev. Mater.* **2016**, *1*, 16009.
(8) Liu, H. L.; Nosheen, F.; Wang, X. Noble Metal Alloy Complex Nanostructures: Controllable Synthesis and Their Electrochemical Property. *Chem. Soc. Rev.* **2015**, *44*, 3056−3078.
(9) Chaudhari, N. K.; Joo, J.; Kim, B.; Ruqia, B.; Choi, S. I.; Lee, K. Recent Advances in Electrocatalysts toward the Oxygen Reduction Reaction: the Case of PtNi Octahedral. *Nanoscale* **2018**, *10*, 20073−20088.
(10) Liu, M.; Zhao, Z.; Duan, X.; Huang, Y. Nanoscale Structure Design for High-Performance Pt-Based ORR Catalysts. *Adv. Mater.* **2019**, *31*, 1802234.
(11) Zhao, Z.; Chen, C.; Liu, Z.; Huang, J.; Wu, M.; Liu, H.; Li, Y.; Huang, Y. Pt-Based Nanocrystal for Electrocatalytic Oxygen Reduction. *Adv. Mater.* **2019**, *31*, 1808115.
(12) Stamenkovic, V. R.; Fowler, B.; Mun, B. S.; Wang, G.; Ross, P. N.; Lucas, C. A.; Markovic, N. M. Improved Oxygen Reduction Activity on Pt_3Ni (111) *via* Increased Surface Site Availability. *Science* **2007**, *315*, 493−497.
(13) van der Vliet, D. F.; Wang, C.; Li, D.; Paulikas, A. P.; Greeley, J.; Rankin, R. B.; Strmcnik, D.; Tripkovic, D.; Markovic, N. M.; Stamenkovic, V. R. Unique Electrochemical Adsorption Properties of Pt-Skin Surfaces. *Angew. Chem., Int. Ed.* **2012**, *51*, 3139−3142.
(14) Zhang, S.; Zhang, X.; Jiang, G.; Zhu, H.; Guo, S.; Su, D.; Lu, G.; Sun, S. Tuning Nanoparticle Structure and Surface Strain for Catalysis Optimization. *J. Am. Chem. Soc.* **2014**, *136*, 7734−7739.
(15) Jia, Q.; Caldwell, K.; Strickland, K.; Ziegelbauer, J. M.; Liu, Z.; Yu, Z.; Ramaker, D. E.; Mukerjee, S. Improved Oxygen Reduction Activity and Durability of Dealloyed $PtCo_x$ Catalysts for Proton Exchange Membrane Fuel Cells: Strain, Ligand, and Particle Size Effects. *ACS Catal.* **2015**, *5*, 176−186.
(16) Bu, L.; Zhang, N.; Guo, S.; Zhang, X.; Li, J.; Yao, J.; Wu, T.; Lu, G.; Ma, J. Y.; Su, D.; Huang, X. Biaxially Strained PtPb/Pt Core/Shell Nanoplate Boosts Oxygen Reduction Catalysis. *Science* **2016**, *354*, 1410−1414.
(17) Luo, M.; Guo, S. Strain-Controlled Electrocatalysis on Multimetallic Nanomaterials. *Nat. Mater. Rev.* **2017**, *2*, 17059.
(18) Chattot, R.; Asset, T.; Bordet, P.; Drnec, J.; Dubau, L.; Maillard, F. Beyond Strain and Ligand Effects: Microstrain-Induced Enhancement of the Oxygen Reduction Reaction Kinetics on Various PtNi/C Nanostructures. *ACS Catal.* **2017**, *7*, 398−408.
(19) Xia, Z.; Guo, S. Strain Engineering of Metal-Based Nanomaterials for Energy Electrocatalysis. *Chem. Soc. Rev.* **2019**, *48*, 3265−3278.
(20) Lim, B.; Jiang, M.; Camargo, P. H. C.; Cho, E. C.; Tao, J.; Lu, X.; Zhu, Y.; Xia, Y. Pd-Pt Bimetallic Nanodendrites with High Activity for Oxygen Reduction. *Science* **2009**, *324*, 1302−1305.
(21) Oezaslan, M.; Hasché, F.; Strasser, P. Oxygen Electroreduction on $PtCo_3$, PtCo and Pt_3Co Alloy Nanoparticles for Alkaline and Acidic PEM Fuel Cells. *J. Electrochem. Soc.* **2012**, *159*, B394−B405.
(22) Zhu, H.; Zhang, S.; Guo, S.; Su, D.; Sun, S. Synthetic Control of FePtM Nanorods (M = Cu, Ni) to Enhance the Oxygen Reduction Reaction. *J. Am. Chem. Soc.* **2013**, *135*, 7130−7133.
(23) Choi, D. S.; Robertson, A. W.; Warner, J. H.; Kim, S. O.; Kim, H. Low-Temperature Chemical Vapor Deposition Synthesis of Pt-Co Alloyed Nanoparticles with Enhanced Oxygen Reduction Reaction Catalysis. *Adv. Mater.* **2016**, *28*, 7115−7122.
(24) Luo, M.; Sun, Y.; Yingjun, Y.; Yang, Y.; Wu, D.; Guo, S. Boosting Oxygen Reduction Catalysis by Tuning the Dimensionality of Pt-Based Nanostructures. *Acta Phys. -Chim. Sin.* **2018**, *34*, 361−376.
(25) Roy, C.; Knudsen, B. P.; Pedersen, C. M.; Velázquez-Palenzuela, A.; Christensen, L. H.; Damsgaard, C. D.; Stephens, I. E. L.; Chorkendorff, I. Scalable Synthesis of Carbon-Supported Platinum-Lanthanide and Rare-Earth Alloys for Oxygen Reduction. *ACS Catal.* **2018**, *8*, 2071−2080.
(26) Qin, Y.; Luo, M.; Sun, Y.; Li, C.; Huang, B.; Yang, Y.; Li, Y.; Wang, L.; Guo, S. Intermetallic *hcp*-PtBi/*fcc*-Pt Core/Shell Nanoplates Enable Efficient Bifunctional Oxygen Reduction and Methanol Oxidation Electrocatalysis. *ACS Catal.* **2018**, *8*, 5581−5590.
(27) Liu, C.; Ma, Z.; Cui, M.; Zhang, Z.; Zhang, X.; Su, D.; Murray, C. B.; Wang, J. X.; Zhang, S. Favorable Core/Shell Interface within Co_2P/Pt Nanorods for Oxygen Reduction Electrocatalysis. *Nano Lett.* **2018**, *18*, 7870−7875.
(28) Feng, Q.; Zhao, S.; He, D.; Tian, S.; Gu, L.; Wen, W.; Chen, C.; Peng, Q.; Wang, D.; Li, Y. Strain Engineering to Enhance the Electrooxidation Performance of Atomic-Layer Pt on Intermetallic Pt_3Ga. *J. Am. Chem. Soc.* **2018**, *140*, 2773−2776.
(29) Wang, Z.; Yao, X.; Kang, Y.; Miao, L.; Xia, D.; Gan, L. Structurally Ordered Low-Pt Intermetallic Electrocatalysts toward Durably High Oxygen Reduction Reaction Activity. *Adv. Funct. Mater.* **2019**, *29*, 1902987.
(30) George, M.; Zhang, G. R.; Schmitt, N.; Brunnengräber, K.; Sandbeck, D. J. S.; Mayrhofer, K. J. J.; Cherevko, S.; Etzold, B. J. M. Effect of Ionic Liquid Modification on the ORR Performance and Degradation Mechanism of Trimetallic PtNiMo/C Catalysts. *ACS Catal.* **2019**, *9*, 8682−8692.
(31) Bu, L.; Ding, J.; Guo, S.; Zhang, X.; Su, D.; Zhu, X.; Yao, J.; Guo, J.; Lu, G.; Huang, X. A General Method for Multimetallic Platinum Alloy Nanowires as Highly Active and Stable Oxygen Reduction Catalysts. *Adv. Mater.* **2015**, *27*, 7204−7212.
(32) Zhu, H.; Zhang, S.; Su, D.; Jiang, G.; Sun, S. Surface Profile Control of FeNiPt/Pt Core/Shell Nanowires for Oxygen Reduction Reaction. *Small* **2015**, *11*, 3545−3549.
(33) Li, M.; Zhao, Z.; Cheng, T.; Fortunelli, A.; Chen, C. Y.; Yu, R.; Zhang, Q.; Gu, L.; Merinov, B. V.; Lin, Z.; Zhu, E.; Yu, T.; Jia, Q.; Guo, J.; Zhang, L.; Goddard, W. A., III; Huang, Y.; Duan, X. Ultrafine Jagged Platinum Nanowires Enable Ultrahigh Mass Activity for the Oxygen Reduction Reaction. *Science* **2016**, *354*, 1414−1419.
(34) Huang, H.; Li, K.; Chen, Z.; Luo, L.; Gu, Y.; Zhang, D.; Ma, C.; Si, R.; Yang, J.; Peng, Z.; Zeng, J. Achieving Remarkable Activity and Durability toward Oxygen Reduction Reaction Based on Ultrathin Rh-Doped Pt Nanowires. *J. Am. Chem. Soc.* **2017**, *139*, 8152−8159.
(35) Mao, J.; Chen, W.; He, D.; Wan, J.; Pei, J.; Dong, J.; Wang, Y.; An, P.; Jin, Z.; Xing, W.; Tang, H.; Zhuang, Z.; Liang, X.; Huang, Y.; Zhou, G.; Wang, L.; Wang, D.; Li, Y. Design of Ultrathin Pt-Mo-Ni Nanowire Catalysts for Ethanol Electrooxidation. *Sci. Adv.* **2017**, *3*, No. e1603068.
(36) Luo, M.; Sun, Y.; Zhang, X.; Qin, Y.; Li, M.; Li, Y.; Li, C.; Yang, Y.; Wang, L.; Gao, P.; Lu, G.; Guo, S. Stable High-Index Faceted Pt Skin on Zigzag-Like PtFe Nanowires Enhances Oxygen Reduction Catalysis. *Adv. Mater.* **2018**, *30*, 1705515.
(37) Zhang, N.; Feng, Y.; Zhu, X.; Guo, S.; Guo, J.; Huang, X. Superior Bifunctional Liquid Fuel Oxidation and Oxygen Reduction Electrocatalysis Enabled by PtNiPd Core-Shell Nanowires. *Adv. Mater.* **2017**, *29*, 1603774.
(38) Li, K.; Li, X.; Huang, H.; Luo, L.; Li, X.; Yan, X.; Ma, C.; Si, R.; Yang, J.; Zeng, J. One-Nanometer-Thick PtNiRh Trimetallic Nanowires with Enhanced Oxygen Reduction Electrocatalysis in Acid

https://dx.doi.org/10.1021/acscatal.9b04419
ACS Catal. 2020, 10, 3018−3026

Media: Integrating Multiple Advantages into One Catalyst. *J. Am. Chem. Soc.* **2018**, *140*, 16159−16167.
(39) Li, C.; Huang, B.; Luo, M.; Qin, Y.; Sun, Y.; Li, Y.; Yang, Y.; Wu, D.; Li, M.; Guo, S. An Efficient Ultrathin PtFeNi Nanowire/Ionic Liquid Conjugate Electrocatalyst. *Appl. Catal., B* **2019**, *256*, 117828.
(40) Stamenkovic, V. R.; Mun, B. S.; Mayrhofer, K. J.; Ross, P. N.; Markovic, N. M. Effect of Surface Composition on Electronic Structure, Stability, and Electrocatalytic Properties of Pt-Transition Metal Alloys: Pt-Skin versus Pt-Skeleton Surfaces. *J. Am. Chem. Soc.* **2006**, *128*, 8813−8819.
(41) Bu, L.; Guo, S.; Zhang, X.; Shen, X.; Su, D.; Lu, G.; Zhu, X.; Yao, J.; Guo, J.; Huang, X. Surface Engineering of Hierarchical Platinum-Cobalt Nanowires for Efficient Electrocatalysis. *Nat. Commun.* **2016**, *7*, 11850.
(42) Gong, M.; Deng, Z.; Xiao, D.; Han, L.; Zhao, T.; Lu, Y.; Shen, T.; Liu, X.; Lin, R.; Huang, T.; Zhou, G.; Xin, H.; Wang, D. One-Nanometer-Thick Pt_3Ni Bimetallic Alloy Nanowires Advanced Oxygen Reduction Reaction: Integrating Multiple Advantages into One Catalyst. *ACS Catal.* **2019**, *9*, 4488−4494.
(43) Huang, X.; Zhao, Z.; Cao, L.; Chen, Y.; Zhu, E.; Lin, Z.; Li, M.; Yan, A.; Zettl, A.; Wang, Y. M.; Duan, X.; Mueller, T.; Huang, Y. High-Performance Transition Metal-Doped Pt_3Ni Octahedra for Oxygen Reduction Reaction. *Science* **2015**, *348*, 1230−1234.
(44) Beermann, V.; Gocyla, M.; Willinger, E.; Rudi, S.; Heggen, M.; Dunin-Borkowski, R. E.; Willinger, M. G.; Strasser, P. Rh-Doped Pt-Ni Octahedral Nanoparticles: Understanding the Correlation between Elemental Distribution, Oxygen Reduction Reaction, and Shape Stability. *Nano Lett.* **2016**, *16*, 1719−1725.
(45) Lim, J. H.; Shin, H.; Kim, M. J.; Lee, H.; Lee, K. S.; Kwon, Y. K.; Song, D. H.; Oh, S. K.; Kim, H.; Cho, E. A. Ga-Doped Pt-Ni Octahedral Nanoparticles as a Highly Active and Durable Electrocatalyst for Oxygen Reduction Reaction. *Nano Lett.* **2018**, *18*, 2450−2458.
(46) Liang, J.; Li, N.; Zhao, Z.; Ma, L.; Wang, X.; Li, S.; Liu, X.; Wang, T.; Du, Y.; Lu, G.; Han, J.; Huang, Y.; Su, D.; Li, Q. Tungsten-Doped $L1_0$-PtCo Ultrasmall Nanoparticles as High-Performance Fuel Cell Cathode. *Angew. Chem., Int. Ed.* **2019**, *58*, 15471−15477.
(47) Sümer, A.; Aksoylu, A. E. Effect of Platinum Incorporation on the Energetics and Oxygen Chemisorption Properties of the Ni(111) Surface. *ChemCatChem* **2012**, *4*, 2005−2012.
(48) Kresse, G.; Furthmüller, J. Efficient Iterative Schemes for Ab Initio Total-Energy Calculations Using a Plane-Wave Basis Set. *Phys. Rev. B: Condens. Matter Mater. Phys.* **1996**, *54*, 11169−11186.
(49) Perdew, J. P.; Burke, K.; Ernzerhof, M. Generalized Gradient Approximation Made Simple. *Phys. Rev. Lett.* **1996**, *77*, 3865−3868.
(50) Blöchl, P. E. Projector Augmented-Wave Method. *Phys. Rev. B: Condens. Matter Mater. Phys.* **1994**, *50*, 17953−17979.
(51) Monkhorst, H. J.; Pack, J. D. Special Points for Brillonin-Zone Integrations. *Phys. Rev. B* **1976**, *13*, 5188−5192.
(52) Gao, L.; Li, X.; Yao, Z.; Bai, H.; Lu, Y.; Ma, C.; Lu, S.; Peng, Z.; Yang, J.; Pan, A.; Huang, H. Unconventional p-d Hybridization Interaction in PtGa Ultrathin Nanowires Boosts Oxygen Reduction Electrocatalysis. *J. Am. Chem. Soc.* **2019**, *141*, 18083−18090.
(53) Nørskov, J. K.; Rossmeisl, J.; Logadottir, A.; Lindqvist, L.; Kitchin, J. R.; Bligaard, T.; Jónsson, H. Origin of the Overpotential for Oxygen Reduction at a Fuel-Cell Cathode. *J. Phys. Chem. B* **2004**, *108*, 17886−17892.
(54) Stamenkovic, V.; Mun, B. S.; Mayrhofer, K. J. J.; Ross, P. N.; Markovic, N. M.; Rossmeisl, J.; Greeley, J.; Nørskov, J. K. Changing the Activity of Electrocatalysts for Oxygen Reduction by Tuning the Surface Electronic Structure. *Angew. Chem., Int. Ed.* **2006**, *45*, 2897−2901.

https://dx.doi.org/10.1021/acscatal.9b04419
ACS Catal. 2020, 10, 3018−3026